Influence of sintering temperature on conductivity and mechanical behavior of the solid electrolyte LATP

Gang Yan[1*], Shicheng Yu[2], Juliane Franciele Nonemacher[1], Hermann Tempel[2], Hans Kungl[2], Jürgen Malzbender[1†], Rüdiger-A. Eichel[2,3,4], Manja Krüger[1]

[1] Forschungszentrum Jülich GmbH, Institute of Energy and Climate Research, Microstructure and Properties of Materials (IEK-2), 52425 Jülich, Germany

[2] Forschungszentrum Jülich GmbH, Institute of Energy and Climate Research, Fundamental Electrochemistry (IEK-9), 52425 Jülich, Germany

[3] Forschungszentrum Jülich GmbH, Ionics in Energy Storage (IEK-12), 48149 Münster, Germany

[4] RWTH Aachen, Institute of Physical Chemistry, 52074 Aachen, Germany

Abstract

To warrant long-term reliability for application of electrolytes in solid state batteries also mechanical properties have to be considered. Current work concentrates on $Li_{1+x}Al_xTi_{2-x}(PO_4)_3$ (LATP), which based on its conductivity is a very promising material. Effect of sintering temperature (950, 1000, 1050, 1100 °C) on mechanical properties and conductivity was tested. Impedance tests were carried out and as main focus of the work the mechanical behavior of LATP samples was determined. The impedance tests results revealed that LATP sintered at 1100 °C had the highest ion conductivity. The LATP sintered at 1100 °C revealed also the highest elastic modulus and hardness, which appeared to be related mainly to a smaller lattice

---

[*] g.yan@fz-juelich.de; tel: +492461616477.; fax: ++492461613699

[†] j.malzbender@fz-juelich.de; tel: +492461616964.; fax: ++492461613699

parameter with additional effects of lower porosity especially when tested at higher loads. The results indicate that enhancement of both mechanical behavior and conductivity requires lowering secondary phase content and densifying the microstructure of the material.

Keywords: Battery; solid electrolyte; sintering temperature; mechanical properties; fracture toughness;

1. Introduction

The good energy capacity of lithium-ion batteries (LIBs) makes them promising electrochemical energy storage devices [1, 2]. In fact, the demand for LIBs is strongly increasing due to the boost of the portable devices market and potential for automotive applications [3]. However, in conventional LIBs, the liquid electrolyte is a flammable organic solvent. This solvent has become a big challenge for the development of the LIBs, since it can lead to toxic fluid leakage or even chemical reaction that can result in an explosion [4]. Recently, solid Li-ion conducting ceramic electrolytes have received considerable attention, since they combine high ionic conductivity with low electrical conductivity, chemical stability and potentially sufficient mechanical properties [5, 6]. In fact, ceramic materials with the structure of NASICON are known to possess a high ionic conductivity [7, 8], and, in particular, the $Li_{1+x}Al_xTi_{2-x}(PO_4)_3$ (LATP) ceramic is one of the most promising candidates for the solid state LIBs application [9-11].

Regarding the application of solid electrolytes, studies mainly focused on the electro-chemical properties. Nevertheless, during operation of the lithium batteries, expansion and contractions of the electrodes and Li metal penetration can lead to the failure of the electrolyte, which indicates that the mechanical characteristics, besides fracture behavior especially the elastic modulus, need to be considered [12-14]. In addition, the electrolyte supported lithium battery cell requires a sufficient resistance against deformation that is also related to the materials' hardness [15, 16].

It has been reported that, to some degree, the currently considered solid electrolyte also suffers from effects related to the temperature applied during sintering, stoichiometric repeatability, grain boundary blocking effect and also electrochemical uncertainty [9, 11, 17-20].

However, these disadvantages affect not only the ionic conductivity of the electrolyte; they can also affect the mechanical properties, which determine safety and lifetime of the lithium batteries. For example, Nonemacher et al. reported recently for LLZO electrolytes sintering at 1150 °C and 1200 °C different lattice parameters and phase ratios, which resulted in differences in mechanical properties [6].

There are a number of publications on mechanical aspects of solid electrolytes [5, 21-25], yet few concentrated on LATP. Jackman et al. [26] reported on micro-cracking influence on ionic conductivity, which indicated that fine-grained LATP had twice the ionic conductivity of a coarse-grained LATP due to reduced fracture at grain boundaries.

Elastic modulus of the LATP material obtained via biaxial test ranged from 81 to 115 GPa. The fracture toughness of LATP material tested via the SENB method was 1.1 ± 0.3 $\mathrm{MPa \cdot m^{1/2}}$. Cutler et al. [27] reported that the biaxial fracture stresses of LATP after exposure to different solutions ranged from 144 to 191 MPa, possessing much higher values than after exposure to air (26 MPa). Hence, overall, the solid electrolytes LATP is expected to possess not only good conductivity, but also acceptable mechanical properties to resist deformation, crack or dendrite growth.

The indentation test method is widely used for characterization of the mechanical properties of materials [28-32] and has already been used to evaluate the properties of solid electrolyte materials [6, 20]. In the current work, the mechanical behavior, including the elastic modulus (E), hardness (H) and fracture toughness (K_{IC}), of the solid electrolyte LATP (hot-pressed, sintered at different temperatures) are investigated via the indentation. A complementary outlook on the correlation of mechanical properties and ionic conductivity is added.

2. Experimental

$Li_{1+x}Al_xTi_{2-x}(PO_4)_3$ (LATP) was chosen because of its good chemical stability and high ionic conductivity [9-11]. The processing of the material follows the procedures outline in [17]. Firstly, LATP powder was prepared by a traditional sol-gel synthetic approach. In this method, 25 ml of $Ti(OC_3H_8)_4$ and 50 ml NH_4OH (Aldrich, 30% solution) were mixed to produce a gelatinous. In order to remove the redundant base, deionized water was used to wash the precipitate, which was then stored in deionized water. A $H_2[TiO(C_2O_4)_2]$ solution was produced with addition of 200 ml of 1 M oxalic acid (Aldrich, 99.9%). Then the solution was mixed with $Al(NO_3)_3$ $9H_2O$ (Aldrich, 99.9%), $(NH_4)_2HPO_4$ (Aldrich, 98%) and excess $LiCOOCH_3$ $2H_2O$ (Aldrich, 98%) and stirred. A hot plate (temperature 80 °C) was used to heat up the mixed solution to remove the water to gain the mixed precursors. Then a pre-annealing was carried out for the mixture for 5 h at 850 °C in air. Thereafter the powders were grinded and filled into a uniaxial die of 11 mm diameter for pressing with 40 kN. Subsequently the cylinder was pressed for 10 s with an isostatic load of 1425 kN and then sintered at different temperatures in the range 950 °C to 1100 °C.

Microstructures of the LATP samples and the indentation imprints for calculating the fracture toughness were acquired by scanning electron microscopy (SEM: Zeiss SUPRA 50VP). To analysis the phase and obtain structural information X-ray diffraction (XRD) was done via a Bruker 4 Endeavour spectrometer. For the XRD test Cu-K_α radiation was used and the scanning range was 10° to 130° with the step of $\Delta 2\theta = 0.02°$ and 2 s. Two different methods were applied to measure the porosity of the LATP samples. The first method was based on defining the bulk density from mass and geometry volume. Then the relative density was calculated as the rate of the bulk density divided by the theoretical density of 2.92 g/cm^3 for LATP (x = 0.3) [33]. In the second method the porosity was terminated by the pore volume fraction via image analysis. Furthermore, the LATP samples' grain size was determined from SEM images with the software "AnalySIS pro". The mean value of the grain size was defined by probing the amount of the intercepts generated by test lines and circles through grain boundary trails within the chosen images [34].

For electrical contacting, LATP pellets with 0.31 mm thickness were polished to remove the potentially contaminated as-sintered surface and make the surface smooth, and then gold layers were sputtered on both sides. A potentiastat (Bio-Logic, SP-300) was used to measure the impedance, where the frequency range was 7 MHz to 1 Hz and the amplitude 10 mV. The tests were conducted in a climate chamber at room temperature of 25 °C. The ionic conductivity was calculated by the following relationship:

$$\sigma = L/R_b S \tag{1}$$

where R_b, L, S and are the bulk electrolyte resistance, the thickness of the electrolyte and the contact area of the interfaces, respectively. For each sintering temperature one LATP sample was used for the impedance test. For the ionic conductivity calculation L was 0.31 mm, where S decreased in the range 1.089 to 1.004 cm^2 and R_b decreased in the range 327.4 to 174.3 Ohm.

To obtain *E, H* and K_{IC} via indentation test, the LATP pellets were embedded in water free resin and again polished to remove the potentially contaminated as-sintered surface and make the surface smooth. Specimens were polished with sandpaper from 400 to 5000 grit and using polishing suspensions of water-free Polyethylene Glycol (PEG) mixed with 0.2 µm SiO_2. Using a polishing system without water permitted to protect the LATP samples from proton/lithium transaction as a result of absorbed water, hence the mechanical properties were not affected by moisture.

The indentation test is a method that is frequently used for gauging the mechanical properties of ceramic materials and particularly in the energy area [20, 35]. In this work the indentation tests were conducted with a Fischerscope H100C (Helmut Fischer KG, Sindelfingen) with a Vickers tip. Various loads (5, 10, 30, 50, 100, 300, 500 mN) were applied to obtain the *E* and *H* of the LATP. At each load 20 indentations were performed to get a representative average and standard deviation. Hold period and acquisition rate during the tests were 1 s and 10 Hz, respectively. Dependence of *E* and *H* on load of the LATP samples will be shown to assess any potential variability in mechanical characteristics. *E* and *H* were evaluated based on the Oliver and Pharr methodology from the indentation load-displacement curve [29], considering a Poisson's ratio v of 0.24 for LATP [36].

The fracture toughness of the LATP samples was obtained with the aid of a micro-hardness tester (Buehler Micromet 1) based on the conventional Vickers indentation method [37]. In order to obtain well-defined indentation imprints a load of 0.5 N was applied. Six indentations and holding times of 20 s were employed to induce the cracks. The crack lengths associated with the

Vickers imprints were analyzed directly after test via SEM to prevent any bias by subcritical crack growth as well effects related to moisture in the air.

To derive the fracture toughness, the cracks lengths originating from the indentation corners and the diagonals were measured. In general, the suitable model for calculating K_{IC} depends on the crack type [38]. In this work the equation derived by Lawn and Evans (P being the load) was adopted, since the ratio of the measured length of cracks (l) to half of the diagonal (a) matched with the median crack model ($c/a \geq 2.25$ as verified by the experimental data, where $c = a + l$) [39]:

$$K_{IC} = 0.014 \left(\frac{E}{H}\right)^{1/2} \frac{P}{(a+l)^{3/2}} \tag{2}$$

The ratio of elastic modulus to hardness is a parameter in the formula, which in fact, since although both parameters are influenced by the indentation load, is rather independent of the load, as can be seen from the data presented below, for convenience in the current study the values obtained at a load of 500 mN were used.

3. Results and discussion

LATP samples after sintering were characterized via XRD to analyze the phase structure. Via Rietveld refinement, lattice parameters were obtained, which are presented in Table 1. It can be seen that the LATP samples sintered at different temperatures are composed of LATP in rhombohedral structure as a main phase and only some minor amount of secondary phase. In fact, with increase of the sintering temperature, the amount of the secondary phase also increased. The secondary phase can be a result of Li^+ evaporation from LATP during high temperature sintering, since as Li^+ evaporated the Al^+ dopant level might have exceeded the solubility limit and precipitates formed [40, 41]. From the lattice parameter it can be seen that a^* and b^* are similar for all four samples, whereas the c^* parameter yielded decreasing values as the sintering temperature increased. Overall, the lattice parameter results agreed with that reported by Swati et al.[42], where $a^* = b^* = 0.8512$ nm, $c^* = 2.0878$ nm.

The microstructures of the materials synthesized at different temperatures are shown in Fig. 1. An EDX result of the LATP sintered at 1100 °C is also presented in Fig. 1 to indicate the distribution of the secondary phase $AlPO_4$. All LATP samples possess a porous structure. The grain size of the LATP specimens were 9.5 ± 5.2, 9.7 ± 5.1, 10.5 ± 6.0 and 12.1 ± 5.9 μm for sintering temperatures of 950, 1000, 1050 and 1100 °C, respectively. Hence, the average of grain size of the samples increased slightly with rising sintering temperature, being in consistent with that reported by Duluard et al. [33]. The pores were spherical inside those grains, while irregular at the boundaries. In addition, the amount of the pores inside the grains decreased as the sintering temperature increased. The elements O and P were distributed uniformly in the sample as shown in Fig. 1(e), whereas the Al-rich region (without titanium) can be assigned to the $AlPO_4$ phase, which agglomerated. The $AlPO_4$ phase existed in mainly grain boundaries, which is in good agreement with that reported by Yu et al.[17].

Three different methods for porosity measurement were adopted and compared to acquire the relative density of the LATP samples, since the porosity can affect the mechanical properties of the materials like elastic modulus, hardness and fracture toughness [43, 44]. Porosities of LATP based on the Archimedes' theory were derived via immersion in water (data referred to [17]). Hence, the geometric (physical) measurement results are representative of the bulk density. Besides, the densities from the image analysis were obtained from the Fig. 1, which were selected rather dense areas of the samples.

The Archimedes' porosity is much lower than that from the other methods, since only the open porosity was exposed to water, while the relative density of image analysis is a little bit higher than that of the physical measurement, which might be attributed to the chosen rather dense area. It's not the scope of the work to analyze local difference by considering a lot of microstructure pictures, for example a detailed analysis of pore effects is presented in the work of Ying et al. [45]. From the results in Table 2 it can be concluded that, with increasing of the sintering temperature, the porosity of the samples decreased. The lower porosity of the samples sintered at higher temperatures was expected due to the extrusion of bubbles.

Regarding conductivity, since the layer thickness as well as contact between the sample and gold layer can influence the ion transport, it was more appropriate to compare the total conductivity of LATP samples according to the specific geometries.

The ionic conductivity results based on an equivalent circuit model obtained at 25 °C are shown in Fig. 2, where the impedance spectroscopy curves are given as inserted. As shown in the figure, the left intercept points are in the same position, which means the conductivity of the grains is same for all samples. However, the conductivity of the grain boundaries appears to be different. The sintering temperature increase led to a conductivity increase from 8.69×10^{-5} to

1.83×10^{-4} S/cm, i.e. specimens sintered at 1100 °C had the highest conductivity. Hence, it can be recognized that the sintering temperature indeed affects the conductivity, as indicated mainly due to grain boundary effects. Key et al. [40] suggested that a higher density and larger grain size can decrease the grain boundary impedance, while a secondary phase of $AlPO_4$ at grain boundaries can limit the total conductivity.

The elastic moduli of the LATP samples sintered at different temperatures as a function of load are exhibited in Fig. 3. It can be seen that for all samples the elastic modulus decreases with increasing indentation load. An exponential curve was used in the current work as guide to the eye to emphasis the continuous decrease of the elastic moduli being stronger in the lower load range and then stabilizing at higher loads. Note that, the curves are only a guide for the eye and they do not imply a fitting with a physical meaning.

The decrease of E with load (corresponding to depth and hence increasing deformed volume) can be related to a porosity effect and in particular for the lower sintering temperatures, effect of weak grain boundaries, i.e. as load increases the effectively deformed zone of the indentation enlarges leading then to a response of dense material and defects. At load of 5 mN, the elastic moduli of LATP samples sintered at different temperature were 127 ± 5, 130 ± 6, 131 ± 7 and 135 ± 8 GPa, respectively, being basically representative of the property of the dense material.

According to the graphical representation of the data, the elastic modulus of LATP sintered at 950 °C is lower than that of all others and overall, the elastic modulus slightly increases with the sintering temperature. For higher loads, this can be ascribed to the lower porosity at higher sintering temperature, since the pores can decrease the elastic modulus of a material. For the lowest load, the smaller lattice parameter c^* will be the main factor for the higher E values for higher sintering temperatures. It has already been shown for other materials that the mean elastic modulus increased with a decrease of lattice parameter [46, 47]. Additional grain size effects can be ruled out, since the grain size is in the same range for all materials tested in the current work.

For comparison, the reported elastic modulus of $AlPO_4$ is around 77 GPa [48, 49], which due to its existence as second phase might influence the elastic modulus of LATP, especially leading to differences for specimens sintered at high temperatures. However, the experimental results indicate that the lattice parameter dominates, leading to an increase in elastic modulus, over any potential decrease of the elastic modulus owning to the secondary phase with increasing sintering temperature (see also Table 1).

The hardness of the LATP materials that were sintered at different temperatures was also tested at different loads. The hardness results are presented in Fig. 4. At the low load of 5 mN, the hardness values of LATP sintered at different temperatures are 10.1 ± 0.1, 10.5 ± 0.4, 11.0 ± 0.5 and 11.5 ± 0.8 GPa, respectively. From Fig. 4, it can be seen that the hardness of LATP sintered at 950 °C is the lowest, whereas those of the other three samples are rather similar. As a guide for the eye the exponential curves were used to indicate that the hardness decreased continuously stabilized at higher loads. Again these curves are only guidance guide to the eye and they don’t imply any physical meaning of the fitting.

The decrease of this property with increasing load can also be associated with a porosity effect, since also the plastic zone increases at higher loads. Overall, the hardness of materials is affected by four features. One of them is the porosity of the material [50]. The porosity of the LATP samples decreases with increasing sintering temperature, which indicates that the hardness of the LATP should be higher at higher sintering temperatures, however, similar as in case of elastic modulus this should be mainly an effect at higher loads. Second is the lattice parameter of the material. It has been reported that the hardness of materials can be correlated to the shear and bulk modulus [51, 52]. The shear modulus and bulk modulus are also key parameters related to the yield strength, which increases as the lattice parameter decreases. Thus, a smaller lattice parameter c^* can be a factor for the higher H values of LATP sintered at higher temperature, especially at lower loads where a pronounced effect of the pores cannot be expected. Thirdly, the grain size of the samples, i.e. it has been reported that as the grain size becomes larger the hardness decreases [53, 54]. The grain size of the four samples in current work was in a similar range. The fourth is the difference of the type as well as the amount of secondary phase. The amount of the second phase of LATP got higher as the sintering temperature rose. The secondary phase $AlPO_4$ was partially distributed inside the grain. As reported the Mohs hardness of $AlPO_4$ is around 6.5 [55] and the microhardness 3.5 - 5.5 GPa [56], hence, the LATP sintered in high temperature that possessed a higher amount of secondary phases should yield a lower hardness especially at high loads due to the large effective zone. Although the secondary phase $AlPO_4$ can lower the hardness, porosity and lattice parameter had a contrary effect on the LATP's hardness.. Increasing the density of the LATP during sintering can enhance the hardness, which might be a benefit for the application.

In order to characterize the type of bonding, the ratio of hardness to shear modulus, G (can be calculated as $G = E/2(1 + v)$), was used as a parameter. Apparently the ratio H/G of 0.1, H/G of

0.01 and *H*/*G* of 0.001 can indicate covalent, ionic and metallic bonding, respectively [57, 58]. As mentioned above, the Poisson's ratio *v* is 0.24 [36], so together with the elastic modulus and hardness the dominant bonding type of LATP materials can be determined. The *H*/*G* value was calculated for LATP sintered at different temperatures as being 0.20, 0.20, 0.21 and 0.20, respectively. This suggested that the LATP samples are mainly governed by a covalent bonding type, which agrees well with that published for LATP (~0.16) [59] and other perovskite and garnet materials [59], i.e. the *H*/*G* value for LLZO is ~0.11 and the *H*/*G* value for LLTO ~0.12.

Fracture toughness was derived in the current work from the length of cracks after indentation. As examples Fig. 5 shows typical Vickers imprints after loading with 0.5 N for LATP sintered at different temperatures. For all specimens indentations at higher load led to crushed material and no crack propagation effects could be studied. Thus only imprints for a load of 0.5 N were considered in the current work. For the LATP synthesized at 950 and 1000 °C, cracks emanated from the corners of the indentations and got stopped at grain boundaries and material partially chipped out in the indentation area. Only indentations on LATP sintered at 1050 and 1100 °C left material with remaining global structure integrity and also some cracks with well-defined shape starting from the corners that could be used for fracture toughness determination. Note, only regular straight cracks were considered in the determination of the fracture toughness; cracks that showed interaction with grain boundaries or that extended not in a straight line from the indentation diagonal were not considered.

As mentioned in the experimental part, for calculating the fracture toughness the elastic modulus, hardness and the diagonal length of the indentation imprint as well as the crack length have to be characterized. With a load of 0.5 N, indentations on the LATP 950 °C and 1000 °C were partly crushed, see Fig 5(a) and Fig 5(b). Therefore, it was not possible to derive fracture toughness values for the LATP samples synthesized at 950 °C and 1000 °C. Furthermore, as mentioned above, for the material sintered at higher temperature, to rule out any effect of grain boundaries, cracks intersected with a grain boundary, see Fig. 5 (c), were not considered.

The fracture toughness values of LATP sintered at different temperatures are given in Table 2. As mentioned above, since crack lengths of LATP sintered at lower temperatures were not assessable due to multiple secondary cracks and crack-grain boundary interactions and a fracture toughness was not calculated for these specimens. The derived K_{IC} values of LATP sintered at 1050 °C and 1100 °C were 1.4 ± 0.2 and 1.6 ± 0.2 MPa $m^{1/2}$, respectively.

The ratio of the length of crack to diagonal of the indentation (l/a) was in the range of ((3.1 - 4.4)/(2.4 - 2.8)) and ((4.1 - 5.8)/(2.5 - 2.8)) for LATP synthesized at 1050 °C and 1100 °C, respectively, verifying the validity of the used relationship to derive the data. In order to check the effect of the used crack model, the equation for Palmqvist cracks [60] was also used as a complementary study yielding for example for LATP 1100 °C a K_{IC} of 1.75 ± 0.3 MPa $m^{1/2}$ at 0.5 N, which is close to the 1.6 ± 0.2 MPa $m^{1/2}$ for the radial mode, hence verifying that the result is rather insensitive of the used crack mode model.

Obviously, the results also verify that the LATP materials are brittle. With application of the external load, brittle materials can show catastrophic failure owing to the low intrinsic fracture toughness (typically up to 3 MPa $m^{1/2}$) [61].

It can be seen that the fracture toughness of LATP sintered at 1100 °C is slightly larger than the fracture toughness of the one sintered at 1050 °C. Since indentations and cracks for LATP sintered at 1050 °C and 1100 °C that were considered in the analysis were mainly located inside a single grain (at least for the visible surface), the fracture toughness is probably not affected much by the grain size or the grain boundaries. Nevertheless a possible factor of the microstructure influencing the K_{IC} could be the porosity, since pores are typically located also inside grains.

Generally, materials have a higher fracture toughness for lower porosities [62]. As seen from Fig. 1, the amount of pores inside grains of LATP sintered 1100 °C appears to be less than that in case of the material sintered at 1050 °C. However, since pore – crack interactions were not visible after the indentation impression and porosity was rather low, main reason for the difference can also be related to differences in fracture energy that is on one side directly linked to the fracture toughness and on the other side directly linked to the bonding strength and hence, similar as the elastic modulus, to the lattice parameter.

Elastic modulus, hardness and fracture toughness of LATP obtained in the current work can be compared also with data reported elsewhere and also those of some other solid electrolytes. It has been reported that the elastic modulus of $LiTi_2(PO_4)_3$ type electrolytes calculated from first principle is 139.0 – 152.5 GPa[36], which agrees well with the data obtained here, but being higher than those reported by Jackman et al. (81 – 115 GPa) [26]. Compared with the work of Jackman et al.[26], the hardness values derived here are higher (7.1 ± 0.4 GPa). The elastic modulus and hardness differences compared to the work of Jackman et al.[26] can be partly attributed to the test method, i.e. Jackman et al. used biaxial and flexural tests, which means the effectively deformed zone was much larger than the indentation test adopted here, hence potentially resulting in stronger porosity effects. The fracture toughness values derived here are in good accordance with their value of 1.1 ± 0.3 MPa m$^{1/2}$, considering experimental uncertainties.

For the garnet-type electrolyte $Li_{6.19}Al_{0.27}La_3Zr_2O_{12}$, with 97% density and 5 μm grain size, an elastic modulus of 150 ± 0.4 GPa has been reported [63]. For perovskite-type electrode $Li_{0.33}La_{0.57}TiO_{12}$, with 99% density and 1.5-13 μm grain size, the reported elastic moduli were in the range of 143 to 203 GPa [64]. Hence, the currently tested LATP materials have a lower elastic modulus than $Li_{6.19}Al_{0.27}La_3Zr_2O_{12}$ and $Li_{0.33}La_{0.57}TiO_{12}$. Compared with literature, the current LATP materials possess a similar hardness as the garnet-type electrolyte $Li_{6.19}Al_{0.27}La_3Zr_2O_{12}$ [63] (9.1 ± 0.5 GPa) and the perovskite-type electrode $Li_{0.33}La_{0.57}TiO_{12}$ [64] (8.1 to 8.4 GPa). In current literature [63, 64], the K_{IC} of garnet-type electrolyte $Li_{6.19}Al_{0.27}La_3Zr_2O_{12}$ is reported to be 1.25 ± 0.32 MPa m$^{1/2}$ and the K_{IC} of perovskite-type electrode $Li_{0.33}La_{0.57}TiO_{12}$ as 1.15 to 1.24 MPa m$^{1/2}$ [63, 64]. This indicates that the fracture toughness of LATP sintered at 1100 °C is slightly higher than that of $Li_{6.19}Al_{0.27}La_3Zr_2O_{12}$ and $Li_{0.33}La_{0.57}TiO_{12}$.

In the present work it is shown that the conductivity at 25 °C and the mechanical performances, i.e. elastic modulus, hardness and fracture toughness, of LATP sintered at 1100 °C are higher than those for the material sintered at lower temperatures. This appears to be promising for the application of LATP materials, since good ion-conductivity behavior and mechanical properties can be obtained simultaneously. Yu et al. [17] suggest that, to reduce the resistance of LATP material, the secondary phase ($AlPO_4$) content and microstructure needed to be adjusted: less secondary phase, larger grain size and denser microstructure. Since the elastic modulus as well as hardness of $AlPO_4$ are both lower than that of LATP materials, it might be speculated that lowering the content of $AlPO_4$ can also improve the mechanical properties of LATP even further. In addition, porosity also influences the mechanical properties significantly, especially when considering the macroscopic elastic modulus and even fracture stress as global property.

4. Conclusions

Mechanical properties and ionic conductivity of LATP sintered at different temperatures (950, 1000, 1050, 1100 °C) were characterized in this work at room temperature. The grain sizes of the four samples were similar, whereas both, the amount of secondary phase and density increased as sintering temperature rose. LATP sintered at 1100 °C showed the highest conductivity of 1.83×10^{-4} S/cm. The elastic moduli of the LATP samples were 127 ± 5, 130 ± 6, 131 ± 7 and 135 ± 8 GPa, respectively. The hardness values of LATP sintered at different temperatures were 10.1 ± 0.1, 10.5 ± 0.4, 11.0 ± 0.5 and 11.5 ± 0.8 GPa, respectively. The higher elastic modulus and hardness value at low load of LATP sintered at higher temperature was related to the increase of lattice parameter c^*. The decreasing of the elastic modulus and hardness with the increasing of load was related mainly to a porosity effect. The fracture toughness, K_{IC}, of LATP sintered at 1050 and 1100 °C were 1.4 ± 0.2 and 1.6 ± 0.2 MPa $m^{1/2}$, respectively. The value for the LATP sintered at a higher temperature was slightly higher, probably again due to the lattice parameter. The exact correlation between the lattice parameter c^* and the mechanical properties appear to be promising for future studies.

Obviously to confirm effects of the porosity on the mechanical characteristics global properties obtained via higher indentation loads or optional impulse excitation or bending tests would be an asset in forthcoming studies. However, main aim should be to obtain materials in the densest possible state, rendering values obtained at low loads rather important. Overall, this work provides a database for further improvement of LATP materials to gain both suitable mechanical properties and conductivity by lowering the secondary phase content and densifying the microstructure of the material.

Acknowledgements

The authors would like to thank Ms. T. Osipova for the technical support. Dr. E. Wessel and Mr. M. Ziegner aided the work with microstructural and compositional analysis. Gang Yan acknowledges the funding from the China Scholarship Council (CSC) of China and Juliane F. Nonemacher acknowledges the support from the National Council for Scientific and Technological Development (CNPq) of Brazil.

References

[1] B. Scrosati, J. Garche, Lithium batteries: Status, prospects and future, J Power Sources, 195 (2010) 2419-2430.

[2] L. Grande, E. Paillard, J. Hassoun, J.B. Park, Y.J. Lee, Y.K. Sun, S. Passerini, B. Scrosati, The lithium/air battery: still an emerging system or a practical reality?, Adv Mater, 27 (2015) 784-800.

[3] M. Armand, J.-M. Tarascon, Building better batteries, Nature, 451 (2008) 652-657.

[4] K. Takada, Progress and prospective of solid-state lithium batteries, Acta Mater, 61 (2013) 759-770.

[5] A.-N. Wang, J.F. Nonemacher, G. Yan, M. Finsterbusch, J. Malzbender, M. Krüger, Mechanical properties of the solid electrolyte Al-substituted $Li_7La_3Zr_2O_{12}$ (LLZO) by utilizing micro-pillar indentation splitting test, J Eur Ceram Soc, (2018).

[6] J.F. Nonemacher, C. Hüter, H. Zheng, J. Malzbender, M. Krüger, R. Spatschek, M. Finsterbusch, Microstructure and properties investigation of garnet structured $Li_7La_3Zr_2O_{12}$ as electrolyte for all-solid-state batteries, Solid State Ionics, 321 (2018) 126-134.

[7] H. Wu, G. Chan, J.W. Choi, I. Ryu, Y. Yao, M.T. McDowell, S.W. Lee, A. Jackson, Y. Yang, L. Hu, Stable cycling of double-walled silicon nanotube battery anodes through solid–electrolyte interphase control, Nature nanotechnology, 7 (2012) 310.

[8] P. Verma, P. Maire, P. Novák, A review of the features and analyses of the solid electrolyte interphase in Li-ion batteries, Electrochim Acta, 55 (2010) 6332-6341.

[9] J. Narváez-Semanate, A. Rodrigues, Microstructure and ionic conductivity of $Li_{1+x}Al_xTi_{2\ x}(PO_4)_3$ NASICON glass-ceramics, Solid State Ionics, 181 (2010) 1197-1204.

[10] W. Zhou, S. Wang, Y. Li, S. Xin, A. Manthiram, J.B. Goodenough, Plating a dendrite-free lithium anode with a polymer/ceramic/polymer sandwich electrolyte, J Am Chem Soc, 138 (2016) 9385-9388.

[11] Y. Shao, F. Ding, J. Xiao, J. Zhang, W. Xu, S. Park, J.G. Zhang, Y. Wang, J. Liu, Making Li ‐ air batteries rechargeable: Material challenges, Adv Funct Mater, 23 (2013) 987-1004.

[12] P. Balakrishnan, R. Ramesh, T.P. Kumar, Safety mechanisms in lithium-ion batteries, J Power Sources, 155 (2006) 401-414.

[13] H. Tavassol, E.M. Jones, N.R. Sottos, A.A. Gewirth, Electrochemical stiffness in lithium-ion batteries, Nat Mater, 15 (2016) 1182.

[14] C. Monroe, J. Newman, The impact of elastic deformation on deposition kinetics at lithium/polymer interfaces, J Electrochem Soc, 152 (2005) A396-A404.

[15] Y. Wang, J. Travas-Sejdic, R. Steiner, Polymer gel electrolyte supported with microporous polyolefin membranes for lithium ion polymer battery, Solid State Ionics, 148 (2002) 443-449.

[16] R. Moshtev, B. Johnson, State of the art of commercial Li ion batteries, J Power Sources, 91 (2000) 86-91.

[17] S. Yu, A. Mertens, X. Gao, D.C. Gunduz, R. Schierholz, S. Benning, F. Hausen, J. Mertens, H. Kungl, H. Tempel, Influence of microstructure and $AlPO_4$ secondary-phase on the ionic conductivity of $Li_{1.3}Al_{0.3}Ti_{1.7}(PO_4)_3$ solid-state electrolyte, Functional Materials Letters, 9 (2016) 1650066.

[18] V. Epp, Q. Ma, E.-M. Hammer, F. Tietz, M. Wilkening, Very fast bulk Li ion diffusivity in crystalline $Li_{1.5}Al_{0.5}Ti_{1.5}(PO_4)_3$ as seen using NMR relaxometry, Phys Chem Chem Phys, 17 (2015) 32115-32121.
[19] S. Tao, J.T. Irvine, A stable, easily sintered proton - conducting oxide electrolyte for moderate - temperature fuel cells and electrolyzers, Adv Mater, 18 (2006) 1581-1584.
[20] X. Hu, X. Cheng, S. Qin, G. Yan, J. Malzbender, W. Qiang, B. Huang, Mechanical and electrochemical properties of cubic and tetragonal $Li_xLa_{0.557}TiO_3$ perovskite oxide electrolytes, Ceram Int, 44 (2018) 1902-1908.
[21] K. Kerman, A. Luntz, V. Viswanathan, Y.-M. Chiang, Z. Chen, practical challenges hindering the development of solid state Li ion batteries, J Electrochem Soc, 164 (2017) A1731-A1744.
[22] G. Bucci, T. Swamy, Y.-M. Chiang, W.C. Carter, Modeling of internal mechanical failure of all-solid-state batteries during electrochemical cycling, and implications for battery design, J Mater Chem A, 5 (2017) 19422-19430.
[23] L.L. Baranowski, C.M. Heveran, V.L. Ferguson, C.R. Stoldt, Multi-Scale Mechanical Behavior of the Li3PS4 Solid-Phase Electrolyte, Acs Appl Mater Inter, 8 (2016) 29573-29579.
[24] L. Porz, T. Swamy, B.W. Sheldon, D. Rettenwander, T. Frömling, H.L. Thaman, S. Berendts, R. Uecker, W.C. Carter, Y.M. Chiang, Mechanism of lithium metal penetration through inorganic solid electrolytes, Advanced Energy Materials, 7 (2017).
[25] F. Aguesse, W. Manalastas, L. Buannic, J.M. Lopez del Amo, G. Singh, A. Llordés, J. Kilner, Investigating the Dendritic Growth during Full Cell Cycling of Garnet Electrolyte in Direct Contact with Li Metal, Acs Appl Mater Inter, 9 (2017) 3808-3816.
[26] S.D. Jackman, R.A. Cutler, Effect of microcracking on ionic conductivity in LATP, J Power Sources, 218 (2012) 65-72.
[27] S.D. Jackman, R.A. Cutler, Stability of NaSICON-type $Li_{1.3}Al_{0.3}Ti_{1.7}P_3O_{12}$ in aqueous solutions, J Power Sources, 230 (2013) 251-260.
[28] G. Pharr, W. Oliver, Measurement of thin film mechanical properties using nanoindentation, Mrs Bull, 17 (1992) 28-33.
[29] W.C. Oliver, G.M. Pharr, An Improved Technique for Determining Hardness and Elastic-Modulus Using Load and Displacement Sensing Indentation Experiments, J Mater Res, 7 (1992) 1564-1583.
[30] G. Yan, J.F. Nonemacher, H. Zheng, M. Finsterbusch, J. Malzbender, M. Krüger, An investigation on strength distribution, subcritical crack growth and lifetime of the lithium-ion conductor $Li_7La_3Zr_2O_{12}$, Journal of Materials Science, 1-11.
[31] J. Malzbender, G. de With, The use of the indentation loading curve to detect fracture of coatings, Surface and Coatings Technology, 137 (2001) 72-76.
[32] J. Malzbender, G. de With, The use of the loading curve to assess soft coatings, Surface and Coatings Technology, 127 (2000) 265-272.
[33] S. Duluard, A. Paillassa, L. Puech, P. Vinatier, V. Turq, P. Rozier, P. Lenormand, P.-L. Taberna, P. Simon, F. Ansart, Lithium conducting solid electrolyte $Li_{1.3}Al_{0.3}Ti_{1.7}(PO_4)_3$ obtained via solution chemistry, J Eur Ceram Soc, 33 (2013) 1145-1153.
[34] R.T. DeHoff, F.N. Rhines, Quantitative microscopy, (1968).
[35] A. Chanda, B. Huang, J. Malzbender, R. Steinbrech, Micro-and macro-indentation behaviour of $Ba_{0.5}Sr_{0.5}Co_{0.8}Fe_{0.2}O_{3\ d}$ perovskite, J Eur Ceram Soc, 31 (2011) 401-408.

[36] Z. Deng, Z. Wang, I.-H. Chu, J. Luo, S.P. Ong, Elastic properties of alkali superionic conductor electrolytes from first principles calculations, J Electrochem Soc, 163 (2016) A67-A74.
[37] F. Sergejev, M. Antonov, Comparative study on indentation fracture toughness measurements of cemented carbides, Proc. Estonian Acad. Sci. Eng, 12 (2006) 388-398.
[38] M. Sebastiani, K. Johanns, E.G. Herbert, G.M. Pharr, Measurement of fracture toughness by nanoindentation methods: Recent advances and future challenges, Current Opinion in Solid State and Materials Science, 19 (2015) 324-333.
[39] B.R. Lawn, A. Evans, D. Marshall, Elastic/plastic indentation damage in ceramics: the median/radial crack system, J Am Ceram Soc, 63 (1980) 574-581.
[40] B. Key, D.J. Schroeder, B.J. Ingram, J.T. Vaughey, Solution-based synthesis and characterization of lithium-ion conducting phosphate ceramics for lithium metal batteries, Chem Mater, 24 (2012) 287-293.
[41] R. Kali, A. Mukhopadhyay, Spark plasma sintered/synthesized dense and nanostructured materials for solid-state Li-ion batteries: Overview and perspective, J Power Sources, 247 (2014) 920-931.
[42] S. Soman, Y. Iwai, J. Kawamura, A. Kulkarni, Crystalline phase content and ionic conductivity correlation in LATP glass–ceramic, J Solid State Electr, 16 (2012) 1761-1766.
[43] R.O. Silva, J. Malzbender, F. Schulze-Küppers, S. Baumann, O. Guillon, Mechanical properties and lifetime predictions of dense $SrTi_{1-x}Fe_xO_{3-\delta}$ (x= 0.25, 0.35, 0.5), J Eur Ceram Soc, 37 (2017) 2629-2636.
[44] J. Magdeski, The porosity dependence of mechanical properties of sintered alumina, Journal of the University of Chemical Technology and Metallurgy, 45 (2010) 143-148.
[45] Y. Zou, J. Malzbender, Development and optimization of porosity measurement techniques, Ceram Int, 42 (2016) 2861-2870.
[46] M. Liu, B. Shi, J. Guo, X. Cai, H. Song, Lattice constant dependence of elastic modulus for ultrafine grained mild steel, Scripta Mater, 49 (2003) 167-171.
[47] W. Son, H. Gao, T. Duong, A. Talapatra, M. Radovic, R. Arróyave, Effect of A mixing on elastic modulus, cleavage stress, and shear stress in the $Ti_3(Si_xAl_{1\ x})C_2$ MAX phase, Phys Rev B, 95 (2017) 235131.
[48] V. Shpakov, J. Tse, V. Belosludov, R. Belosludov, Elastic moduli and instability in molecular crystals, Journal of Physics: Condensed Matter, 9 (1997) 5853.
[49] Y. Zhou, B. Liu, Theoretical investigation of mechanical and thermal properties of MPO_4 (M= Al, Ga), J Eur Ceram Soc, 33 (2013) 2817-2821.
[50] J. Wolfenstine, J. Allen, J. Read, J. Sakamoto, G. Gonalez-Doncel, Hot-pressed $Li_{0.33}La_{0.57}TiO_3$, J Power Sources, 195 (2010) 4124-4128.
[51] D. Labonte, A.-K. Lenz, M.L. Oyen, On the relationship between indentation hardness and modulus, and the damage resistance of biological materials, Acta biomaterialia, 57 (2017) 373-383.
[52] X.-Q. Chen, H. Niu, D. Li, Y. Li, Modeling hardness of polycrystalline materials and bulk metallic glasses, Intermetallics, 19 (2011) 1275-1281.
[53] R. Spriggs, Effect of Open and Closed Pores on Elastic Moduli of Polycrystalline Ahmina, J Am Ceram Soc, 45 (1962) 454-454.

[54] R. Chaim, M. Hefetz, Effect of grain size on elastic modulus and hardness of nanocrystalline ZrO_2-3 wt% Y2O3 ceramic, Journal of materials science, 39 (2004) 3057-3061.

[55] J.W. Anthony, Handbook of mineralogy: Arsenates, phosphates, vanadates. arsenates, phosphates, vanadates, Mineral Data Pub.2000.

[56] K. HIROTA, R.C. BRADT, THE MICROHARDNESS INDENTATION SIZE/LOAD EFFECT (ISE) IN SINGLE-CRYSTAL, BERLINITE, Advanced Materials' 93, I, Elsevier1994, pp. 441-444.

[57] J.J. Gilman, The plastic resistance of crystals, Australian Journal of Physics, 13 (1960) 327.

[58] G. Chin, J. Wernick, T. Geballe, S. Mahajan, S. Nakahara, Hardness and bounding in A 15 superconducting compounds, Appl Phys Lett, 33 (1978) 103-105.

[59] J.J. Gilman, Chemistry and physics of mechanical hardness, John Wiley & Sons2009.

[60] A. Evans, T.R. Wilshaw, Quasi-static solid particle damage in brittle solids—I. Observations analysis and implications, Acta Metallurgica, 24 (1976) 939-956.

[61] M.E. Launey, R.O. Ritchie, On the fracture toughness of advanced materials, Adv Mater, 21 (2009) 2103-2110.

[62] R. Rice, Grain size and porosity dependence of ceramic fracture energy and toughness at 22 C, Journal of materials science, 31 (1996) 1969-1983.

[63] J.E. Ni, E.D. Case, J.S. Sakamoto, E. Rangasamy, J.B. Wolfenstine, Room temperature elastic moduli and Vickers hardness of hot-pressed LLZO cubic garnet, Journal of Materials Science, 47 (2012) 7978-7985.

[64] K.G. Schell, F. Lemke, E.C. Bucharsky, A. Hintennach, M. Hoffmann, Microstructure and mechanical properties of $Li_{0.33}La_{0.567}TiO_3$, Journal of Materials Science, 52 (2017) 2232-2240.

Tables Captions

Table 1. Lattice parameter of as-sintered LATP pellets from Rietveld refinement.

Table 2. Comparison of the relative density of LATP samples for the three methods.

Table 3. Fracture toughness of LATP samples sintered at different temperatures.

Table 1. Lattice parameter of as-sintered LATP pellets from Rietveld refinement.

Samples	**Lattice parameters**							
	Space group	*a** (nm)	*b** (nm)	*c** (nm)	α	β	γ	Secondary phase
LATP 950 °C	R-3c h (167)	0.85503	0.85503	2.09859	90°	90°	120°	~ 3.8 wt%
LATP 1000 °C		0.85526	0.85526	2.09702	90°	90°	120°	~ 7.5 wt%
LATP 1050 °C		0.85504	0.85504	2.09777	90°	90°	120°	~ 8.9 wt%
LATP 1100 °C		0.85523	0.85523	2.09652	90°	90°	120°	~ 13.3 wt%

Table 2. Comparison of the relative density of LATP samples for the three methods.

Sample	Archimedes' method [17]	Physical measurement	Image analysis
LATP 950 °C	94.52%	85.7 ± 1.7 %	86.6 ± 0.5 %
LATP 1000 °C	95.48%	87.2 ± 0.9 %	87.3 ± 0.3 %
LATP 1050 °C	96.10%	87.4 ± 0.9 %	90.9 ± 0.7 %
LATP 1100 °C	96.72%	87.9 ± 1.3 %	92.8 ± 0.6 %

Table 3. Fracture toughness of LATP samples sintered at different temperatures.

Sintering temperature	950 °C	1000 °C	1050 °C	1100 °C
Fracture toughness (MPa·$m^{1/2}$)	-	-	1.4 ± 0.2	1.6 ± 0.2

Figures Captions

Fig. 1. SEM and EDX results of LATP. SEM images of LATP samples sintered at different temperatures: (a) 950 °C, (b) 1000 °C, (c) 1050 °C and (d) 1100 °C. (e) element mapping of LATP sintered at 1100 °C.

Fig. 2. Impedance spectroscopy of LATP sintered at different temperatures.

Fig. 3. Elastic modulus of LATP samples as a function of load.

Fig. 4. Hardness of LATP samples as a function of load.

Fig. 5. Typical SEM images of indents on LATP samples, (a), (b), (c) and (d) represent LATP sintered in 950, 1000, 1050 and 1100 °C, respectively.

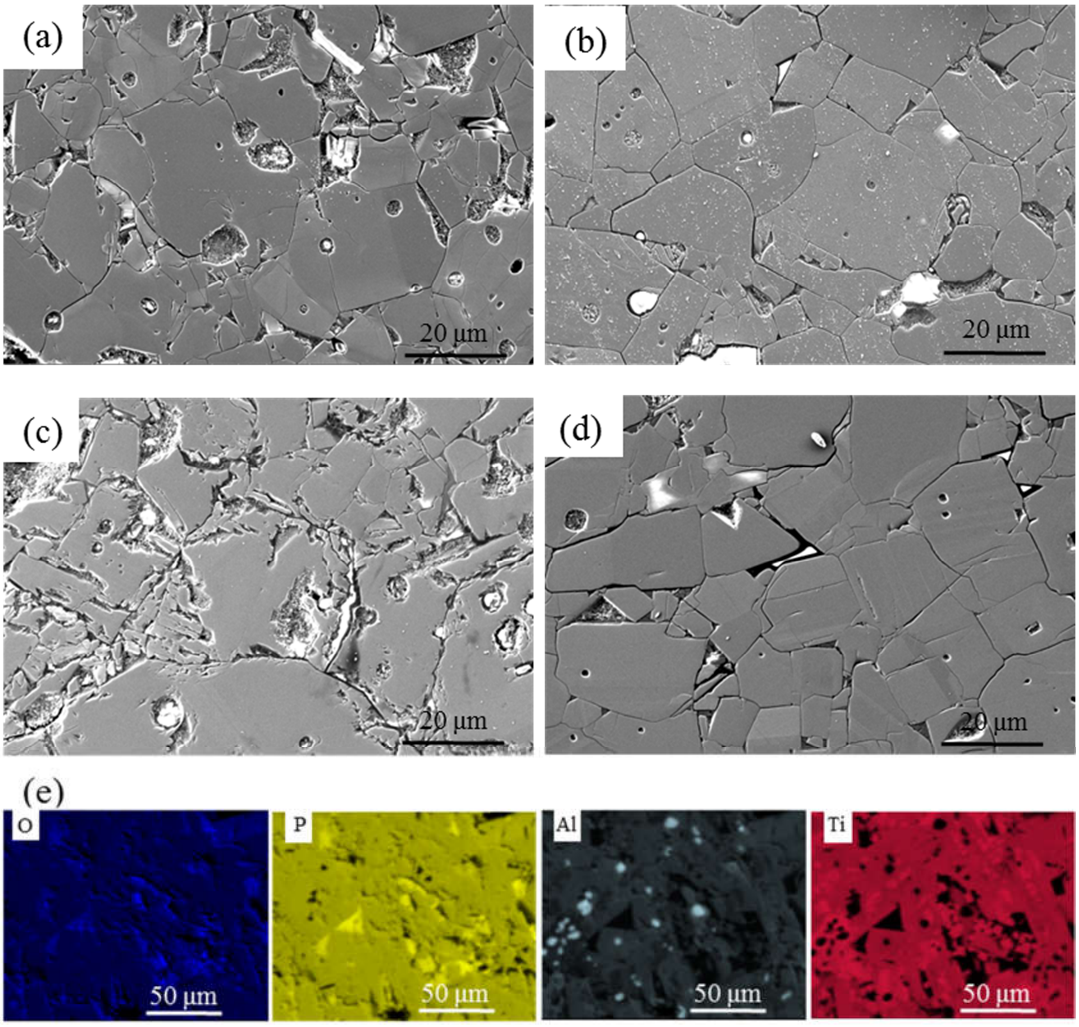

Figure 1. SEM and EDX results of LATP. SEM images of LATP samples sintered at different temperatures: (a) 950 °C, (b) 1000 °C, (c) 1050 °C and (d) 1100 °C. (e) element mapping of LATP sintered at 1100 °C.

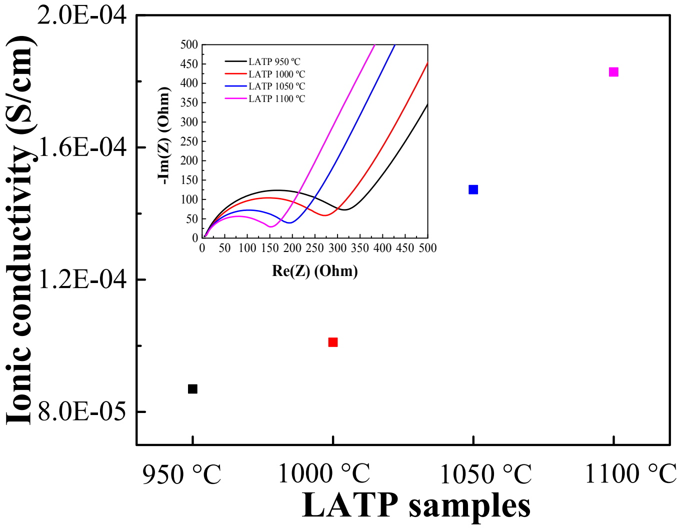

Figure 2. Impedance spectroscopy of LATP sintered at different temperatures.

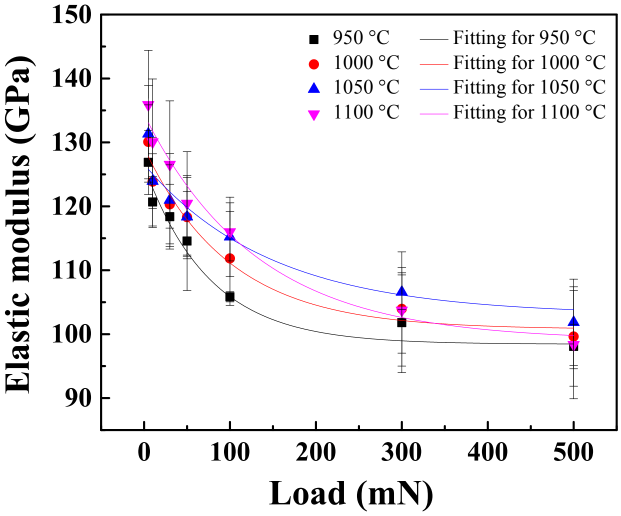

Figure 3. Elastic modulus of LATP samples as a function of load.

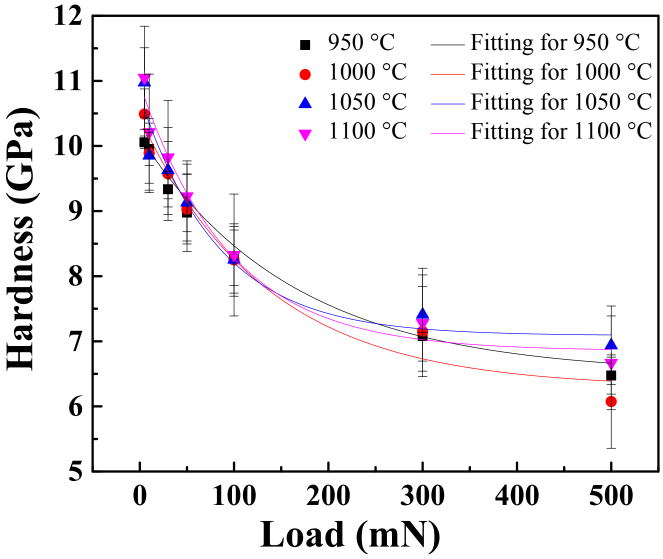

Figure 4. Hardness of LATP samples as a function of load.

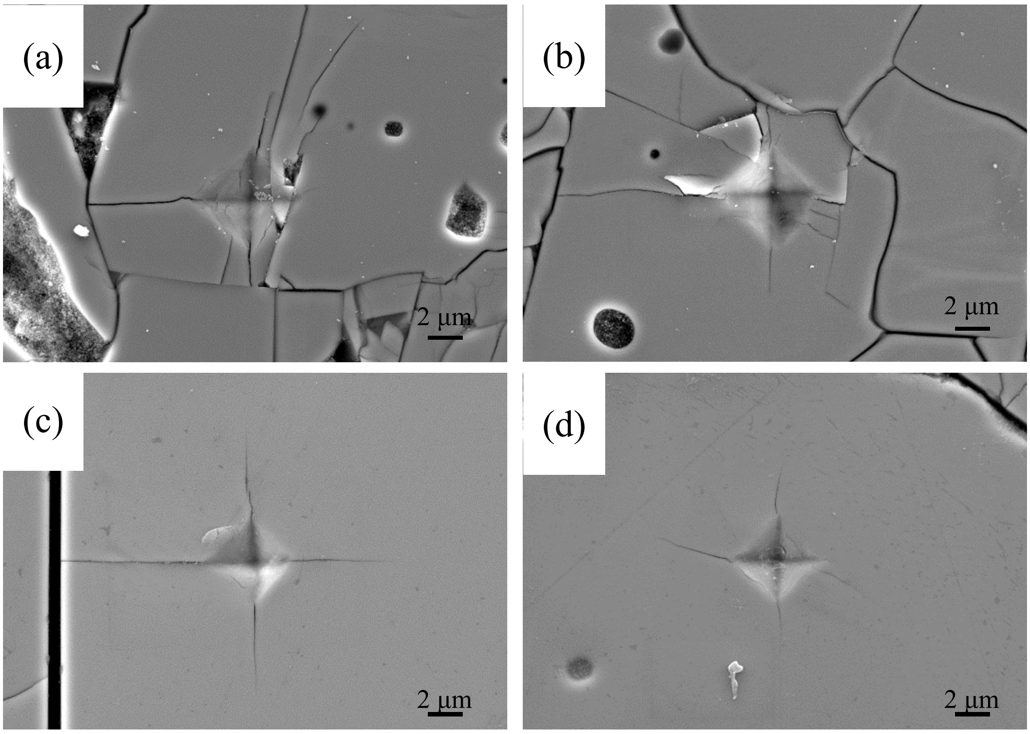

Figure 5. Typical SEM images of indents on LATP samples, (a), (b), (c) and (d) represent LATP sintered in 950, 1000, 1050 and 1100 °C, respectively.